

# Experimental Demonstration of Phase Modulation and Motion Sensing Using Graphene-Integrated Metasurfaces

Nima Dabidian,<sup>†</sup> Shourya Dutta-Gupta,<sup>†</sup> Iskandar Kholmanov,<sup>‡,‡</sup> Kueifu Lai,<sup>†</sup> Feng Lu,<sup>§</sup> Jongwon Lee,<sup>§</sup> Mingzhou Jin,<sup>§</sup> Simeon Trendafilov,<sup>†</sup> Alexander Khanikaev,<sup>||,⊥</sup> Babak Fallahazad,<sup>§</sup> Emanuel Tutuc,<sup>§</sup> Mikhail A. Belkin,<sup>§</sup> and Gennady Shvets<sup>\*,†</sup>

<sup>†</sup>Department of Physics and Center for Nano and Molecular Science and Technology and <sup>‡</sup>Department of Mechanical Engineering and Materials Science Program, The University of Texas at Austin, Austin, Texas 78712, United States

<sup>§</sup>Department of Electrical and Computer Engineering, Microelectronics Research Center, The University of Texas at Austin, 10100 Burnet Road, Austin, Texas 78758, United States

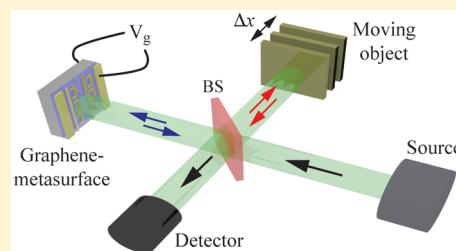
<sup>||</sup>Department of Physics, Queens College of The City University of New York, Queens, New York 11367, United States

<sup>⊥</sup>The Graduate Center of The City University of New York, New York, New York 10016, United States

<sup>\*</sup>CNR-INO, Sensor Lab, The University of Brescia, via Branze 45, 25123, Brescia, Italy

**ABSTRACT:** Strong interaction of graphene with light accounts for one of its most remarkable properties: the ability to absorb 2.3% of the incident light's energy within a single atomic layer. Free carrier injection via field-effect gating can dramatically vary the optical properties of graphene, thereby enabling fast graphene-based modulators of the light intensity. However, the very thinness of graphene makes it difficult to modulate the other fundamental property of the light wave: its optical phase. Here we demonstrate that considerable phase control can be achieved by integrating a single-layer graphene (SLG) with a resonant plasmonic metasurface that contains nanoscale gaps. By concentrating the light intensity inside of the nanogaps, the metasurface dramatically increases the coupling of light to the SLG and enables control of the phase of the reflected mid-infrared light by as much as  $55^\circ$  via field-effect gating. We experimentally demonstrate graphene-based phase modulators that maintain the amplitude of the reflected light essentially constant over most of the phase tuning range. Rapid nonmechanical phase modulation enables a new experimental technique, graphene-based laser interferometry, which we use to demonstrate motion detection with nanoscale precision. We also demonstrate that by the judicious choice of a strongly anisotropic metasurface the graphene-controlled phase shift of light can be rendered polarization-dependent. Using the experimentally measured phases for the two orthogonal polarizations, we demonstrate that the polarization state of the reflected light can be modulated by carrier injection into the SLG. These results pave the way for novel high-speed graphene-based optical devices and sensors such as polarimeters, ellipsometers, and frequency modulators.

**KEYWORDS:** Plasmonic metasurfaces, graphene, phase modulation, polarization modulation, Fano resonance, mid-infrared



Graphene's remarkable electric properties<sup>1–4</sup> and their potential for technological breakthroughs in electronics provided the original impetus to investigating this fascinating two-dimensional atomic crystal. More recently, it has been realized that graphene's optical and plasmonic properties<sup>5,6</sup> can be equally attractive for the development of novel optoelectronic devices. The mid-infrared (mid-IR,  $\lambda \approx 3\text{--}30\ \mu\text{m}$ ) part of the optical spectrum is particularly interesting in the context of graphene-light interactions because graphene has been shown to be a low-loss plasmonic material<sup>7,8</sup> in mid-IR. The main challenge to the integration of graphene into future large-area optoelectronic devices is fundamental: its optical response in mid-IR is weak even in comparison with that in the visible/near-IR and terahertz (THz) parts of the spectrum.<sup>9</sup>

To overcome this limitation, graphene-integrated plasmonic metasurfaces have been recently suggested<sup>8,10–12</sup> as a possible solution. The appeal of plasmonic metasurfaces arises from

their ability to enhance light-matter interaction. The flexibility in the design of these surfaces have already advanced biochemical sensing,<sup>13,14</sup> wavefront engineering,<sup>15,16</sup> and imaging.<sup>17</sup> Metasurface-based ultrathin devices can change the amplitude, polarization, and phase of the light, which are the basic requirements for wavefront engineering and other applications. Conventional optical elements exploit propagation effect to gradually modify the light beam; similarly, metamaterials with spatially varying indices can steer and control light beams resulting in applications such as optical cloaking<sup>18,19</sup> and superlensing.<sup>20</sup> In contrast, metasurfaces can introduce an abrupt change in optical wavefront that originates from the interaction of light with the subwavelength antenna

**Received:** February 19, 2016

**Revised:** April 22, 2016

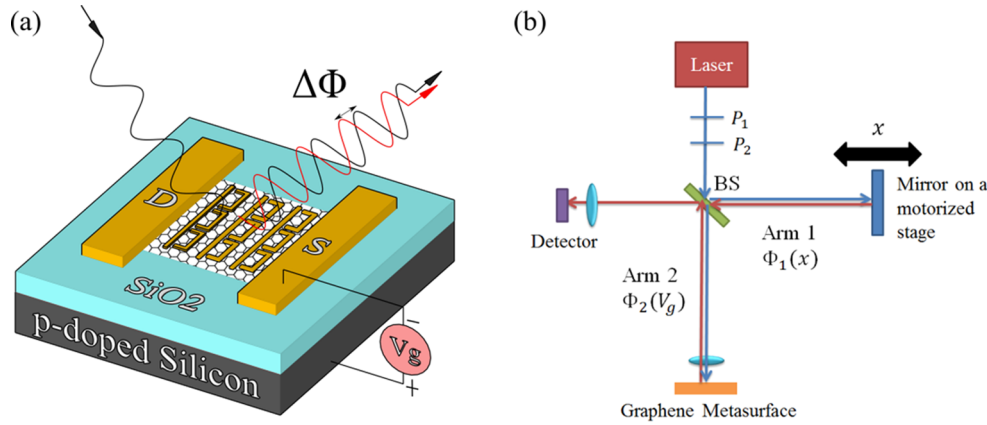


**Figure 1.** (a) Schematic for graphene-induced phase modulation of the reflected light waves. The plasmonic metasurface is fabricated on top of an SLG. Source (S) and drain (D) contacts are attached to SLG for its electrical characterization. The phase modulation  $\Delta\Phi$  is a function of the gate voltage  $V_g$  applied across the insulating  $\text{SiO}_2$  spacer. (b) Experimental setup for the phase measurement: a Michelson interferometer with a beam splitter (BS) and two polarizers  $P_1$  and  $P_2$  used to adjust the power and set the polarization of the infrared beam. The active GIM placed in the test arm (Arm 2) induces a voltage-tunable phase shift  $\Phi_2(V_g)$ , and the moveable mirror on a motorized stage placed in the reference arm (Arm 1) induces a displacement-tunable phase shift  $\Phi_1(x)$ .

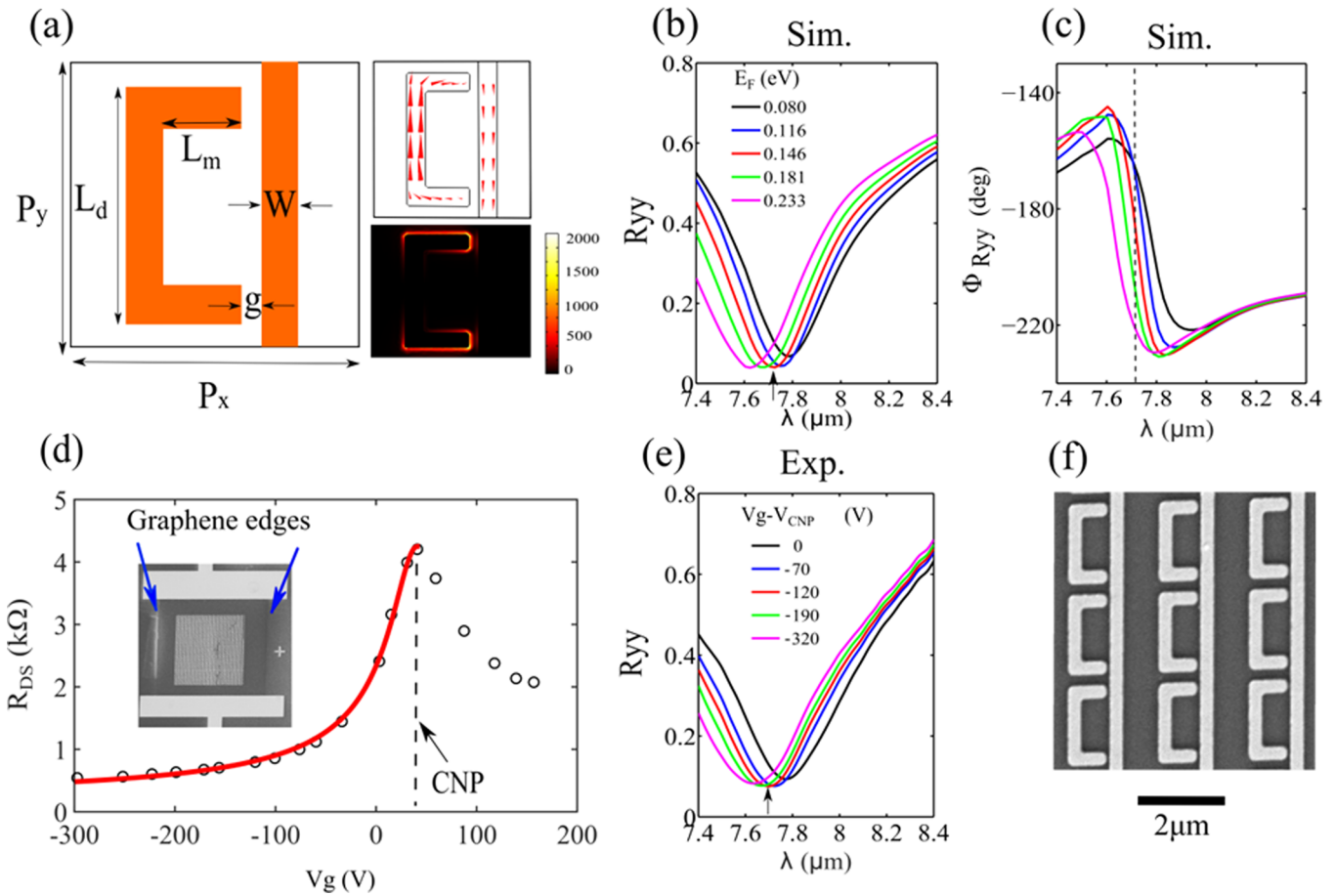


**Figure 2.** (a) The structure of the unit cell of the metasurface, with geometric parameters definitions (left). Top right: current profile in the metal nanoantenna at  $z = 5$  nm above the bottom of the metasurface. Bottom right: near-field enhancement  $\eta = |E_t^2/E_{inc}^2|$  at  $z = 0$ . Currents and fields are simulated at the reflectivity minimum (no underlying graphene). (b) Simulated reflection amplitude and (c) phase for the normally incident y-polarized light as a function of the wavelength  $\lambda$  for different values of graphene's Fermi energy  $E_F$ . The arrow and the dashed line in the panels (b,c), respectively, mark the wavelength corresponding to the reflectivity minimum where the phase measurements are performed. (d) Electrical characterization of graphene under the metasurface: drain-source resistance  $R_{DS}$  as a function of the gate voltage  $V_g$  (markers: experimental data). Vertical dashed line: the gate voltage  $V_{CNP} \approx 40$  V at the charge-neutrality point. Inset: an SEM image of the device showing the metasurface (middle) and drain/source contacts on a graphene sheet. Red curve: analytic fit of  $R_{DS}(V_g)$ . (e) The measured reflection amplitude  $R_{yy}^{(exp)}(\lambda)$  plotted for several values of  $V_g$  and color-coded according to their correspondent  $E_F$  in (b). (f) An SEM image of a segment of the fabricated metasurface. The width of all nanowires are  $W = 250$  nm. Other dimensions:  $g = 120$  nm,  $L_d = 1.8 \mu\text{m}$ ,  $L_m = 600$  nm, and  $P_x = P_y = 2.1 \mu\text{m}$ .

arrays. Such arrays could potentially have spatially varying optical response that provide a greater flexibility in molding the wavefront with applications in holograms,<sup>21–24</sup> beam steering<sup>25</sup> and optical devices such as lenses,<sup>26</sup> axicons,<sup>27</sup> and waveplates.<sup>28</sup> The main drawback of conventional metasurfaces is that they are passive, that is, their optical properties cannot be changed after their fabrication. Therefore, the synergy between plasmonic metasurface and graphene follows from their complementarity: graphene's properties can be reconfigured by applying electric field<sup>1</sup> while metasurfaces can strongly enhance light interaction with graphene. In this Letter, we exploit this synergy and provide the first direct experimental demonstration of phase modulation in mid-IR using graphene-integrated plasmonic metasurfaces.

The technological rationale for using graphene as an electro-optic material comes from the subnanosecond electric response of its optical conductivity to field-effect gating.<sup>8</sup> Graphene-based phase modulators have been demonstrated for telecommunication<sup>29–31</sup> and terahertz wavelengths,<sup>31–34</sup> where graphene's response is strong and primarily resistive. In the more challenging mid-IR part of the spectrum, amplitude modulation<sup>8,10,12,35–38</sup> by as much as an order of magnitude<sup>12,37</sup> has been demonstrated. However, phase modulation remains a challenge despite numerous recent theoretical proposals<sup>12,37,39</sup> and the importance of rapid phase shifting for a broad range of mid-IR applications, including polarimetry, ellipsometry, and frequency modulation. Notably few alternatives to fast graphene-based phase modulation exist in mid-IR. One common platform for phase modulation, liquid crystals,<sup>40</sup> have a millisecond response time and are a challenge to operate in mid-IR range due to liquid crystal light absorption; metamaterial-based solid-state modulators utilizing voltage-controlled carrier depletion in semiconductors have demonstrated megahertz-rate switching speed but only at THz frequencies.<sup>41</sup>

Below we demonstrate that a single-layer graphene (SLG) can significantly shift the phase of the reflected mid-IR light through field-effect gating. The weak optical response of graphene is overcome by integrating it with a Fano-resonant metasurface<sup>42</sup> containing nanoscale gaps where light-graphene interaction is dramatically enhanced. We performed direct measurement of the actively controlled optical phase of the reflected beam by placing our graphene-integrated metasurface (GIM) into one of the arms of a free-space Michelson interferometer as shown in Figure 1. We further demonstrate that the active GIM can be utilized for electrical phase calibration of the remaining arm of the interferometer, thereby providing a potentially rapid motion detection with nanometer-scale accuracy. Finally, we demonstrate that GIMs can be used for active control of light's polarization state (ellipticity), thus paving the way for numerous mid-IR applications to polarization-division multiplexing, active waveplates, fast Stokes polarimetry, and time-resolved ellipsometry.

Our metasurface is designed to exhibit Fano interference and electromagnetically induced transparency<sup>43</sup> (EIT). Plasmonic metasurfaces exhibiting Fano resonances have been shown to exhibit higher near-field concentration of optical energy  $\gamma^{7,12}$  than the standard antenna arrays. The schematic of the metasurface with gating electrodes is shown in Figure 1a and the unit cell details are provided in Figure 2a. The plasmonic nanoantennas are fabricated on top of the SLG grown by the chemical vapor deposition (CVD) and transferred on the SiO<sub>2</sub> insulating spacer on a doped Si substrate (see Methods for

fabrication details). The unit cell consists of a continuous nanowire and a dipole antenna with the same metal stripes width  $W$  placed in close proximity of each other (see the caption to Figure 2 for all physical dimensions). The continuous nanowire emulates a dilute electron plasma and provides a broadband reflectivity from the metasurface for optical waves polarized along the wire, that is, in the  $y$ -direction. Destructive interference between antiparallel currents in the nanowire and in the dipole antenna (Figure 2a, top right panel) that takes place near antenna's plasmonic resonance at  $\lambda = \lambda_D$  causes a dip in reflection (Figure 2b) and the electromagnetically induced transparency (EIT) peak in transmission (not shown). The small gap of the width  $g$  between the antenna and the wire serves two purposes. First, it provides strong capacitive coupling between the two, thereby reducing the natural frequency  $\omega_D \equiv 2\pi c/\lambda_D$  of the resonant dipole excitation and making the antenna strongly subwavelength:  $L_d \ll \lambda_D/2n_{\text{SiO}_2}$ , where  $n_{\text{SiO}_2}$  is the refractive index of the substrate. Second, it concentrates optical energy inside a nanoscale area of the size  $A_{\text{gap}} = g \times W \approx 0.03 \mu\text{m}^2$ .

The nanoscale field concentration in the antenna gap greatly enhances the strength of light-graphene interaction, which is proportional to  $\eta = |E_t^2/E_{\text{inc}}^2|$ ,<sup>12</sup> where  $E_t$  is tangential electric field at the graphene's surface, and  $E_{\text{inc}}$  is the incident  $y$ -polarized electric field. The spatial distribution of the field enhancement  $\eta$  numerically calculated at  $\lambda = \lambda_D \approx 7.7 \mu\text{m}$  and shown in Figure 2a (bottom left panel) reveals  $\eta > 1000$  inside the nanogap. All numerical simulations were carried out using a commercial COMSOL Multiphysics finite-elements frequency-domain package (see Methods for details). To demonstrate the effect of graphene's doping on the position of the Fano resonance of a GIM, we numerically calculated the reflectivity  $R_{yy}(\lambda)$  of normally incident light and plotted the results in Figure 2b for different values of graphene's Fermi energy  $E_F = \hbar v_F \sqrt{\pi n}$  (where  $n$  is the areal free carrier density and  $v_F = 1 \times 10^8 \text{ cm/s}$  is the Fermi velocity<sup>4</sup>). The  $E_F(V_g)$ , in turn, determines the wavelength-dependent optical conductivity  $\sigma_{\text{SLG}}(\lambda, E_F)$  of graphene<sup>43</sup> that was used in our simulations. Significant 2.6% blue-shifting from  $\lambda = 7.8 \mu\text{m}$  (at  $E_F = 0.08 \text{ eV}$ , or  $n = 4.7 \times 11 \text{ cm}^{-2}$ ) to  $\lambda = 7.6 \mu\text{m}$  (at  $E_F = 0.23 \text{ eV}$ , or  $n = 4.0 \times 12 \text{ cm}^{-2}$ ) is predicted by the simulations.

The physics of blue shifting in the Pauli-blocking regime of  $2E_F > \hbar\omega$  is as follows:<sup>7,10</sup> as more carriers are injected into graphene (thereby increasing  $E_F$ ), the imaginary part of graphene's conductivity increases, thereby making graphene more conductive. This has an effect of effectively reducing the inductance of the GIM, thereby increasing its natural resonant frequency. Just as it is the case for any externally driven resonant excitation (the dipole nanoantenna in this case), the amplitude change is followed by the phase change as the natural resonant frequency of the metasurface is swept across the frequency of the incident light. This effect is shown in Figure 2c. Simulations indicate that a phase shift of  $\Delta\Phi_{yy} \approx -60^\circ$  of the reflected light at  $\lambda \approx 7.7 \mu\text{m}$  (dashed line in Figure 2c) should accompany the sweep of the SLG's Fermi energy, which is responsible for sweeping the resonant frequency of the GIM.

Before experimentally measuring the reflectivity spectra  $R_{yy}^{(\text{exp})}(\lambda)$ , graphene was electrically characterized in order to make the connection between  $E_F$  (used in the simulations) and the experimental values of the applied gate voltage  $V_g$ . The drain-source resistivity  $R_{\text{DS}}(V_g)$  measured as a function of the gate voltage is plotted Figure 2d, where the inset shows an

scanning electron microscopy (SEM) image of the fabricated sample. The maximum resistance corresponds to the charge neutrality point (CNP) voltage  $V_{\text{CNP}} \cong 40$  V.<sup>3</sup> The gate voltage applied across the SiO<sub>2</sub> spacer between the silicon substrate and the SLG controls the carrier concentration  $n \approx C_g \Delta V / e$ , where  $\Delta V = V_g - V_{\text{CNP}}$ , and  $C_g = \epsilon / d$  is the gate capacitance per unit area,  $d$  and  $\epsilon$  are the thickness and electrostatic permittivity of the SiO<sub>2</sub> (see Methods for the description of the analytic fit of  $R_{\text{DS}}(V_g)$  shown as the red line in Figure 2d and a more accurate method of calculating  $n$  that accounts for the residual charge density at the CNP) and the related Fermi energy  $E_F(n)$ . A list of the experimentally applied gate voltages and the corresponding graphene's Fermi energies is listed in Table 1.

**Table 1. Fermi Energies  $E_F$  in the SLG and the Corresponding Electric Fields  $E = V_g/d$  Inside the Silicon Oxide Spacer of Thickness  $d = 1$   $\mu\text{m}$  Separating the SLG from the Back Gate Are Tabulated as a Function of the Applied Gate Voltage  $V_g$**

$V_g$ (V)	$E$ (MV/cm)	$E_F$ (eV)
-40	-0.4	0.08
-20	-0.2	0.09
0	0	0.10
30	0.3	0.12
80	0.8	0.15
150	1.5	0.18
280	2.8	0.23

The numerically obtained reflectivity spectra shown in Figure 2b were found to be in good agreement with the experimentally measured spectra  $R_{yy}^{\text{(exp)}}(\lambda)$  that were collected using the optical

setup shown in Figure 1b, where the reference arm (Arm 1) of the interferometer is blocked (see Methods for the details of the measurement). For these measurements,  $y$ -polarized normally incident light produced by a continuously tunable quantum cascade laser (QCL) was used. The gate voltages shown in Figure 2e correspond to the Fermi energies depicted in Figure 2c. Having experimentally confirmed the existence of the EIT-like reflectivity dip and its tuning by electric gating, we now move to the primary objective of this Letter: the measurement of the graphene induced optical phase shift.

A Michelson interferometer configuration was used to measure the phase shift of the IR light that was reflected from the electrically gated GIM placed in the test arm (Arm 2 in Figure 1b) of the interferometer. The laser light is split into two arms by a CaF<sub>2</sub> beam splitter (BS). In Arm 1, the beam is reflected from a mirror mounted on a motorized stage whose motion is controlled by a closed-loop actuator with optical encoding capability. The reflected waves (marked by red arrows in Figure 1b) combined on a mercury–cadmium–telluride (MCT) detector produce the interference electric field that can be expressed as the function of the mirror's position  $x$  and the gate voltage:

$$C(x, V_g, t) = A \sin[\omega t + \Phi_1(x)] + B(V_g) \sin[\omega t + \Phi_2(V_g)] \quad (1)$$

where  $\omega = 2\pi c/\lambda$  is the angular frequency of light,  $A$  and  $\Phi_1(x) = 4\pi x/\lambda + \Phi_1(0)$  are the light's amplitude and phase, respectively, after the passage through Arm 1, and  $\Phi_1(0)$  is a constant phase shift due to the path lengths difference between the two arms. Similarly,  $B(V_g)$  and  $\Phi_2(V_g)$  are, respectively, the

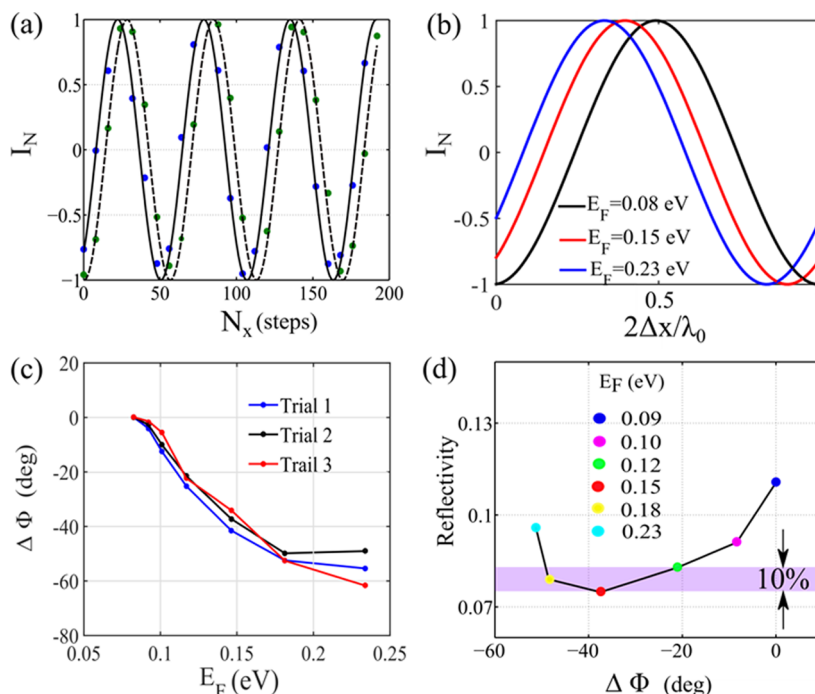


**Figure 3.** (a) Normalized interference signal  $I_N(x = sN_x, V_g)$  for  $V_g = 0$  ( $E_F = 0.1$  eV; green dots, dashed fitted line) and  $V_g = -150$  V ( $E_F = 0.19$  eV; blue dots, solid fitted line). (b) Fitted interference patterns as (a), but plotted for three values of  $E_F$  (black,  $E_F = 0.08$  eV; red,  $E_F = 0.15$  eV; blue,  $E_F = 0.23$  eV) over one oscillation period for the interferometer mirror position shift in the  $0 < sN_x < \lambda_0/2$  range. (c) Phase change  $\Delta\Phi$  as a function of the Fermi energy for three independent experiments (Trials 1–3). (d) Reflectivity-phase diagram using the data from the Trial 1 as a function of color-coded Fermi energy. All measurements are performed at  $\lambda_0 = 7.69$   $\mu\text{m}$ .

amplitude and phase of the light reflected from the graphene-integrated metasurface, both voltage-dependent.

From eq 1, the time-averaged detected intensity is given by  $\langle [C(x, V_g)]^2 \rangle = I_0(V_g) + M(V_g)I_N(x, V_g)$ . Here the background intensity is  $I_0(V_g) = (A^2 + B^2(V_g))/2$ , the depth of the interference signal is  $M(V_g) = AB(V_g)$ , and the normalized oscillatory portion of the interference pattern is  $I_N(x, V_g) = \cos[\Phi_1(x) - \Phi_2(V_g)]$ . The last  $x$ -dependent term is utilized for experimental extraction of the gate-dependent phase shift  $\Phi_2(V_g)$ . Briefly, the measurement procedure of  $\Phi_2$  for any given gate voltage  $V_g = V_1$  is as follows. First, the value of the gate voltage is reset to  $V_g = 0$  to establish the baseline phase shift, and the mirror in the reference arm is advanced from its original  $x = 0$  position through a sequence of  $N_{\max}$  steps while measuring the intensity after each of the  $0 < N_x < N_{\max}$  steps. An example of the interference pattern at  $V_g = 0$  is shown in Figure 3a, where only the normalized quantity  $I_N(x, V_g = 0)$  (green markers) are plotted for several oscillation as a function of  $N_x$  at  $\lambda_0 = 7.69 \mu\text{m}$ . The least-squares fit of the experimental data to  $I_N(x, V_g = 0) = \cos[BN_x + c(0)]$  is shown as a dashed line in Figure 3a, where  $B = 4\pi s/\lambda_0$  is treated as a fitted parameter that depends on the experimentally determined (with better than 0.5% relative accuracy) step size  $s \approx 68 \text{ nm}$ . The same procedure of advancing the mirror from  $x = 0$  to  $x = sN_{\max}$  is repeated for  $V_g = V_1$  as shown in Figure 3a. The blue markers represent the experimental data, and the solid line represents the fitted curve for  $I_N(x, V_g = V_1) = \cos[BN_x + c(V_1)]$ , which is clearly displaced by  $\Delta\Phi(V_1; 0) \equiv \Phi_2(V_1) - \Phi_2(0) = [c(V_1) - c(0)]$  with respect to the  $I_N(x, V_g = 0)$  curve. To our knowledge, the data presented in Figure 3a represents the first direct experimental observation of graphene-induced phase shift of infrared light.

The phase advance  $\Delta\Phi(V_g; 0) = c(V_g) - c(0)$  is calculated for a set of gate voltages (including the CNP voltage  $V_g = V_{\text{CNP}}$ ) using the same procedure outlined above. The gate voltage was reset to  $V_g = 0$  before each measurement in order to avoid the potential hysteretic interfacial effects<sup>44</sup> (e.g., charge trapping and redox reaction) that takes place at high gate voltages. For convenience, in the rest of this Letter we reference all phase shifts to that measured at the CNP voltage. Using the definition of  $c(V_g) = \Phi_1(0) - \Phi_2(V_g)$ , the phase shifts due to free carrier injection into graphene are calculated as

$$\Delta\Phi(V_g) \equiv [\Phi_2(V_g) - \Phi_2(V_{\text{CNP}})] = c(V_{\text{CNP}}) - c(V_g) \quad (2)$$

The results of the interferometric experiments (all performed at  $\lambda = \lambda_0$  indicated by an arrow in Figure 2e and with  $V_g \leq V_{\text{CNP}}$  corresponding to the injection of holes into graphene) are shown in Figure 3b–d, where the gate voltages have been converted to Fermi energies according to Table 1. As an example, three fitted  $I_N(x, V_g)$  for the selected Fermi energies are shown in Figure 3b. The negative phase shift of  $\Delta\Phi(V_g = 280\text{V}) \approx -55^\circ$  (corresponding to  $E_F = 0.23 \text{ eV}$ ) observed from Figure 3b is a direct manifestation of the blue shift of the resonance observed in both simulations (Figure 2b) and experiments (Figure 2e). The measured shift is in good agreement with the results of the numerical simulations shown in Figure 2c.

The robustness and repeatability of the phase shift is confirmed by repeating the experiments three times and plotting the measured phase shifts for the three trials in Figure 3c. We speculate that the repeatability can be further improved by graphene's passivation that can be achieved by, for example,

depositing an insulating layer of  $\text{Al}_2\text{O}_3$ <sup>44,45</sup> or boron nitride (BN)<sup>46</sup> over the SLG and fabricating the metasurface on top of it. Adding a metallic backplane to a GIM may be another attractive option for increasing the phase shift as has been recently theoretically suggested.<sup>37,39</sup>

In Figure 3d, the phase shifts measured during the Trial 1 are replotted in the power reflectivity-reflection phase plane in order to examine the possibility of pure phase modulation with minimal amplitude modulation. The plotted data is color-coded based on the values the Fermi energy of the SLG (see Table 1 for the  $E_F$  versus  $V_g$  conversion), and the phase modulation (PM) region corresponding to 10% variation of the reflectivity  $R_{yy}$  is shaded. The phase shift of the reflected light changes by  $\Delta\Phi_{\text{PM}} \approx -28^\circ$  within the PM region. The property of the pure phase shift at a constant reflectivity is promising for realizing fast phase modulators, as well as in other optical applications. Below, we briefly describe two such applications: interferometric motion detection and polarization conversion.

The concept of interferometric motion detection using an active GIM illustrated in Figure 4a is explained by observing that the test and reference arms of the Michelson interferometer can, in principle, be exchanged. That means that instead of using the known  $\Phi_1(x)$  to measure the unknown

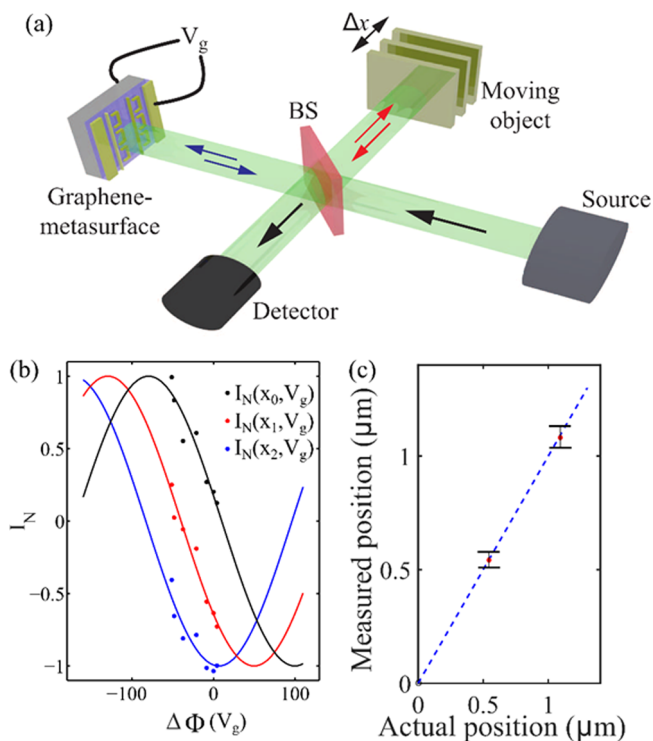


**Figure 4.** (a) Schematic of the interferometric motion detection using a GIM. The motion of the reflecting object (mirror on a moving stage) is detected by varying the phase of the reflected light from the GIM via field-effect gating. (b) Normalized interferograms  $I_N(x_p, V_g)$  plotted for three mirror positions  $x_j = x_0 + j\Delta x$  ( $\Delta x = 540 \text{ nm}$  corresponds to 8 steps of the moving stage,  $j = 0, 1, 2$  for black, red, and blue symbols, respectively) and seven voltages from Table 1. Horizontal axis:  $\Delta\Phi(V_g)$  from Figure 3c (Trial 1). (c) The extracted relative displacements  $(x_1 - x_0)$  and  $(x_2 - x_0)$  are plotted as a function of the actual mirror displacements. The error bar is estimated using six independent sets of position triplets  $x_j$ . Blue dashed line is drawn at  $45^\circ$  to compare the extracted and actual mirror positions. All measurements are performed at  $\lambda = \lambda_0$ .

$\Phi_2(V_g)$ , we can now use the tabulated  $\Phi_2(V_g)$  to measure the unknown  $\Phi_1$ . If an arbitrary reflecting object moving along the  $x = x_{\text{obj}}(t)$  trajectory is used instead of the mirror, then extracting  $\Phi_1(x_{\text{obj}})$  would enable tracking its motion. Such tracking requires that the phase shift  $\Phi_2(V_g)$  in Arm 2 (which becomes the new reference arm) be changed on the time scale which is much shorter than the object's movement. The experimentally obtained plot of  $\Delta\Phi(V_g)$  presented in Figure 3c serves as a look-up table for measuring the movement of the reflecting object (e.g., a moving mirror). The key advantage of the nonmechanical change of  $\Phi_2$  is the speed (tens of GHz) at which such change can be accomplished.

However, there is a significant difference between measuring  $\Phi_2(V_g)$  using a sequence of  $\Phi_1(x_j)$  spanning several periods (where  $0 < x_j < sN_{\text{max}}$ ) as it was done in Figure 3a, and extracting  $\Phi_1(x_{\text{obj}})$  using a sequence of  $\Phi_2(V_g = V_k)$  spanning a fraction of a radian. The accuracy of the latter simulation may be potentially limited because of the smaller phase change in the reference arm. To investigate the spatial resolution of a graphene-based distance measurement interferometer, we have selected six mirror position triplets  $x_j = x_0 + j\Delta x$  (where  $j = 0, 1, 2$ ,  $\Delta x = 0.54 \mu\text{m}$ , and  $x_0$  is different for different triplets) and plotted the normalized interferograms  $I_N(x_j, V_k)$  as a function of for the seven voltages listed in Table 1. The experimental results for one such triplet is shown in Figure 4a, where the black, red, and blue symbols correspond to  $x_0$ ,  $x_1$ , and  $x_2$  members of the triplet, respectively. The data was fitted to  $I_N(x_j, V_k) = \cos[\Psi_j - \Delta\Phi_2(V_k)]$  (solid lines), where  $\Psi_j = 4\pi x_j/\lambda + \Phi_1(0) - \Phi_2(V_{\text{CNP}})$  follows from the definition of  $I_N(x, V_g)$ . Using  $\Psi_j - \Psi_0 = 4\pi(x_j - x_0)/\lambda$ , the relative distances  $(x_1 - x_0)$  and  $(x_2 - x_0)$  were measured and plotted in Figure 4c, and the accuracy (the size of the error bar) was estimated from the results for six independently chosen position triplets  $(x_0, x_1, x_2)$ . Note that this technique does not attempt to extract the absolute distances.

Next, we demonstrated that the accuracy of the displacement measurement is high although the phase change in the reference arm of the interferometer is less than one radian according to Figure 4b. Figure 4c illustrates the accuracy of the measurement by plotting the extracted positions of  $x_1$  and  $x_2$  (referenced to  $x_0$ ) for the six position triplets. The dashed blue line is drawn at  $45^\circ$  to illustrate the agreement between the actual displacements of the mirror (horizontal axis) and the displacement measured using the graphene-based interferometer. The spread between multiple measurements shown in the insets to Figure 4c and the prediction (dashed line) indicate that displacement as small as  $\Delta x = 540 \text{ nm}$  can be measured with  $\pm 40 \text{ nm}$  accuracy. In addition, no assumption of constant (distance-independent) reflectivity from the moving object is needed for the application of this technique. The distance measurement technique based on active GIMs demonstrated above is a potential alternative to the more conventional chirp-based techniques<sup>47</sup> because it is carried out in mid-IR, where atmospheric light scattering is considerably reduced<sup>48</sup> and passive chirping outside of the laser is challenging, and at potentially high (multi-GHz) speeds.

The second application enabled by voltage-controllable GIMs is the development of electrically tunable wave plates that can control the polarization state of the reflected mid-IR light in real time. Because the utilized metasurface (see Figure 2a) is strongly anisotropic, its response to  $x$ -polarized light is very different from the resonant response to  $y$ -polarized light considered so far. Specifically, while strong Fano resonance at  $\lambda$

$= \lambda_0$  occurs for the latter, no such resonance exists for the former. In the absence of resonance, no significant phase variation is expected for reflected  $x$ -polarized light as the gate voltage is varied. This is confirmed by our interferometric measurement, the results of which are described in Figure 5a,

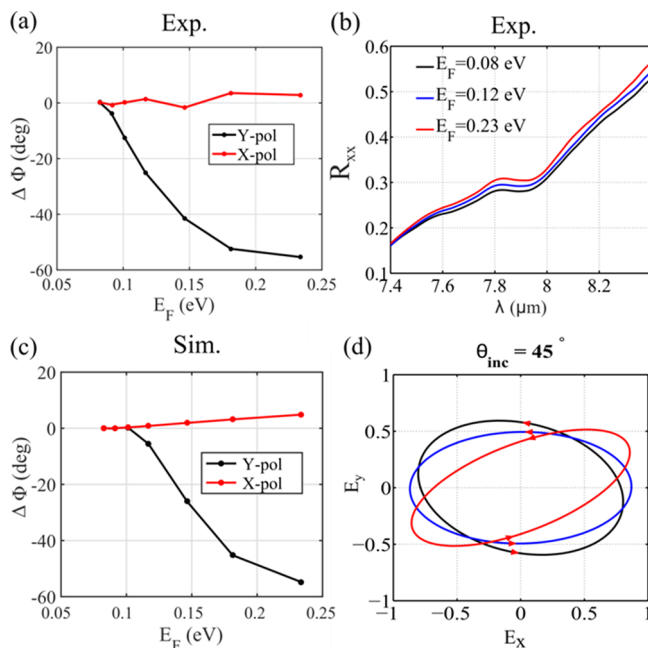


**Figure 5.** (a) Measured phase shifts  $\Delta\Phi_x$  and  $\Delta\Phi_y$  of the linearly polarized light reflected at normal incidence from the voltage-controlled GIM. Red line,  $x$ -polarized; black line,  $y$ -polarized light; horizontal axis, graphene's Fermi energy. (b) Measured reflectivity for  $x$ -polarized incident light corresponding to three Fermi energies. (c) Simulated phase shifts  $\Delta\Phi_x$  and  $\Delta\Phi_y$  plotted as a function of the Fermi energy. (d) Normalized polarization ellipses of the reflected light calculated using eq 3 and the experimentally obtained  $\Delta\Phi_x$  and  $\Delta\Phi_y$  from panel (a). The constant  $\alpha_{\text{CNP}} = 107^\circ$  was extracted from COMSOL simulations. Incident light's polarization at  $45^\circ$  with respect to the principal axes of the metasurface was assumed. The colors correspond to the Fermi energies from panel (b). All measurements and simulations correspond to the wavelength of light ( $\lambda = \lambda_0$ ) that corresponds to the minimum of  $R_{yy}(\lambda)$  at  $E_F = 0.15 \text{ eV}$ . In simulations  $\lambda_0^{(\text{th})} = 7.72 \mu\text{m}$  was used.

where the experimentally obtained phase changes at  $\lambda = \lambda_0$  for both  $x$ - and  $y$ -polarized light at normal incidence are plotted as functions of graphene's Fermi energies  $E_F(V_g)$  taken from Table 1. Both experimentally measured  $\Delta\Phi_x(V_g)$  and  $\Delta\Phi_y(V_g)$  are in good agreement with numerical simulations (Figure 5c). Note that the theoretically and experimentally obtained reflection phases are referenced to those at the CNP point of graphene. The absence of the metasurface's resonant response to  $x$ -polarized light is also experimentally confirmed by featureless reflectivity  $R_{xx}(\lambda)$  that does not appreciably change with  $E_F$  as shown in Figure 5b. Note that the  $x$ - and  $y$ -axes are the principal axes of the metasurface (i.e.,  $R_{xy} = 0$ ) due to the mirror reflection symmetry of the structure with respect to the  $x$ -axis.

The action of an active phase plate is easily captured by examining the polarization state of the reflected light that is polarized at  $45^\circ$  with respect to the principal axes of the GIM at incidence. The resulting (un-normalized) polarization ellipse is given by the following parametric formula

$$E_x(V_g) = \sqrt{R_{xx}} \cos[\alpha_{xy}(V_g) - \omega t], \quad E_y(V_g) = \sqrt{R_{yy}} \cos[\omega t] \quad (3)$$

where  $0 < \omega t < 2\pi$  is a parameter, the two polarized reflectivities ( $R_{xx}$  and  $R_{yy}$ ) may be voltage-dependent, and the reflected phase shift  $\alpha_{xy} = \Delta\Phi_x(V_g) - \Delta\Phi_y(V_g) + \alpha_{\text{CNP}}$  between the two polarizations is also controlled by the gate voltage. Here,  $\alpha_{\text{CNP}} \equiv \Delta\Phi_x(V_{\text{CNP}}) - \Delta\Phi_y(V_{\text{CNP}})$  is the phase shift at the  $V_{\text{CNP}}$ . Here we focus on the case where  $R_{xx}$  and  $R_{yy}$  are nearly voltage-independent as can be observed from the experimental data presented in Figures 2e and 5b. However, the significant (by almost a full radian) voltage-induced  $\Delta\Phi_y$  translates into an equal magnitude shift of  $\alpha_{xy}$  and therefore a significant rotation of the polarization ellipse. Three such normalized polarization ellipses are presented in Figure 5d for the corresponding gate voltages and graphene's Fermi energies extracted from Table 1. These results indicate that both the ellipticity and the orientation of the polarization ellipse can be significantly altered by applying a gate voltage.

For example, we observe from Figure 5d that the direction of the major axis can be moved from the second quadrant (at  $E_F = 0.08$  eV) to the first quadrant (at  $E_F = 0.23$  eV). Note that such orientation of the polarization ellipse is enabled by the voltage-induced phase shift and cannot be accomplished by pure amplitude modulation of either  $R_{xx}(V_g)$  or  $R_{yy}(V_g)$ . This implies that only a limited subspace of Stokes parameters of the reflected light can be accessed by pure amplitude modulation. For example, if the major axis of the polarization ellipse is restricted to stay in the first quadrant, then only the positive values of the second Stokes parameter  $S_2 \equiv I(+45^\circ) - I(-45^\circ)$ , defined as the intensity difference of light passing through the analyzers oriented at  $+45^\circ$  and  $-45^\circ$  with respect to the principal polarization axes, can be accessed. In contrast, phase modulation demonstrated here does not suffer from such restrictions. Therefore, one may envision using phase-shifting graphene-integrated metasurfaces for real-time ellipsometric applications<sup>49</sup> that require high time resolution.

In summary, we have experimentally demonstrated that when a plasmonic metasurface with nanoscale gap features is integrated with single-layer graphene, field-effect gating of the latter can produce large phase changes of the reflected light. By concentrating light's intensity in the nanogaps, the metasurface dramatically induces graphene's coupling to infrared light and enables bias-voltage-control of the reflected waves' phase by over  $50^\circ$ . Such phase shifts were found to be sufficient for two applications: nonmechanical motion sensing with nanometer-scale resolution, and voltage-control of polarization state of reflected mid-IR light. The promise of these and similar applications (such as, for example, real-time ellipsometry using graphene-based polarization state generators) lies in their potential for fast time response. Experimental demonstrations of nanosecond-scale response of graphene-based phase-control metasurfaces will be a subject of future work.

**Methods. Sample Fabrication.** First, the SLG was grown on polycrystalline Cu foil using a CVD technique<sup>50</sup> and subsequently transferred<sup>51</sup> from the Cu foil onto a commercially purchased substrate (University Wafer) with 1  $\mu\text{m}$  thick insulating ( $\text{SiO}_2$ ) layer grown on a lightly doped silicon. Second, the high-quality graphene regions were isolated by e-beam patterning followed by an oxygen plasma cleaning step. Third, a 100  $\mu\text{m} \times 100 \mu\text{m}$  metasurface sample was fabricated on top of the SLG with unit cell dimensions given in Figure 2c using electron beam lithography (EBL). The

thickness of the metasurface was 30 nm (5 nm of Cr and 25 nm of Au). The scanning electron micrograph (SEM) of the fabricated GIM is shown in Figure 2f. Fourth, source and drain contacts (15 nm Cr + 85 nm Au) were deposited on top of graphene on either side of the metasurface samples using a second EBL step. Lastly, a gold contact (15 nm Ni + 85 nm Au) was deposited on the back of the silicon wafer for gating. The fabrication was completed by wire-bonding the sample to a chip carrier. A dc voltage was applied between the source contact and the silicon backgate to modulate graphene's carrier density as shown in Figure 1.

**Electrical Characterization of Graphene.** We used a parametric analyzer (Keithley 2450) for the current–voltage ( $I$ – $V$ ) measurement to characterize the SLG. In Figure 2d the resistance between drain and source contacts  $R_{\text{DS}}$  is shown as a function of gate voltage. This resistance can be written as<sup>45</sup>

$$R_{\text{DS}}(V_g) = R_c + R_g \quad \text{where } N_{\text{sq}} \\ = R_c + N_{\text{sq}}/e\mu_h \sqrt{n_0^2 + [c_g(V_g - V_{\text{CNP}})]^2}$$

$= L_g/W_g$  with  $L_g$  and  $W_g$  being the length and the width of graphene channel.  $\mu_h$  and  $n_0$  represent the graphene hole mobility at room temperature and residual charge of graphene at the CNP point, respectively, and  $c_g$  is the gate capacitance. By fitting the experimentally measured resistance  $R_{\text{DS}}(V_g)$  plotted in Figure 2d to the above expression, the following values for graphene and circuit parameters were extracted:  $R_c = 170 \Omega$ ,  $n_0 = 4.7 \times 10^{11} \text{ cm}^{-2}$  and  $\mu_h = 3600 \text{ cm}^2/(\text{V s})$ .

The CNP  $V_g = V_{\text{CNP}} = 40$  V corresponding to  $n = n_0$  is identified by the maximum value of  $R_{\text{DS}}(V_g)$ . The slight p-doping of the SLG by the  $\text{SiO}_2$  substrate can be inferred from  $V_{\text{CNP}} > 0$ . Because of the breakdown voltage of silicon dioxide at 0.5 GV/m, we varied the back gate voltage in the  $-280 \text{ V} < V_g < 40 \text{ V}$  range using “Heathkit 500 V PS-3” power supply. The holes' areal concentration can reach the maximum values of  $n_h^{\text{max}} \approx 4.0 \times 10^{12} \text{ cm}^{-2}$  for the peak gate voltage. The red curve in Figure 2d demonstrates the fit in the holes' injection regime that is used to extract the graphene's electrical properties. The carrier collisional time is then calculated from mobility using  $\tau = \frac{\sigma_h \hbar^2}{2e^2 E_F} \approx 13$  fs, where the conductivity due to the holes is given by  $\sigma_h = n_h e \mu_h$ .

**Reflectivity Measurements.** The setup shown in Figure 1b was used to measure the optical reflectivity of the sample where the light path in arm 1 was blocked and only the signal from the graphene metasurface was detected. The laser source was a quantum cascade laser (Daylight solution, MIRcat-1400). The laser was operated in pulsed mode with the pulse repetitions rate of 250 kHz and the pulse duration of 100 ns. A high numerical aperture ZnSe lens (NA = 0.5) was used as an objective to focus the laser light onto the metasurface. A liquid-nitrogen-cooled MCT detector was utilized for the measurements of signal intensity. The signal from the MCT detector was amplified and measured by the lock-in amplifier (Stanford research systems SR844) with the integration time of 3 ms.

**Interferometric Measurements.** A Michelson interferometric setup, as shown in Figure 2a, was used to measure the phase modulation. The mirror was mounted on a closed-loop actuator (Newport model 8310) equipped with an optical encoder that provided an accurate and repeatable mirror position measurement. The entire interferogram shown in Figure 3a consisted of 25 points, each separated by 8 actuator steps (the actuators step size:  $s \approx 68$  nm). For measurements, the mirror was stopped

for 200 ms every 8 actuator steps and the MCT detector signal was recorded by the lock-in amplifier with the integration time of 100 ms.

**Numerical Simulations.** A commercial finite elements solver COMSOL Multiphysics version 4.3b was used for simulating the optical reflectivity of the sample. The SLG was modeled using a surface current<sup>7</sup>  $J_{\text{SLG}} = \sigma_{\text{SLG}} E_t$  where  $E_t$  is the tangential electric field on the graphene plane and  $\sigma_{\text{SLG}}$  is the optical conductivity of graphene which was calculated from random-phase approximation in the local limit<sup>52</sup>

$$\sigma_{\text{inter}}(\omega) = \frac{e^2}{4\hbar} \left[ \frac{1}{2} + \frac{1}{\pi} \tan^{-1} \left( \frac{\hbar\omega - 2E_F}{2k_B T} \right) - \frac{i}{2\pi} \ln \frac{(\hbar\omega + 2E_F)^2}{(\hbar\omega - 2E_F)^2 + (2k_B T)^2} \right]$$

$$\sigma_{\text{intra}}(\omega) = \frac{e^2}{4\hbar} \frac{8ik_B T}{\pi\hbar(\omega + i\tau^{-1})} \ln \left[ 2 \cosh \left( \frac{E_F}{2k_B T} \right) \right]$$

For the carrier collisional time, the transport measurement estimation of  $\tau = 13$  fs was used and the temperature was assumed to be  $T = 300$  K.

## AUTHOR INFORMATION

### Corresponding Author

\*E-mail: gena@physics.utexas.edu.

### Author Contributions

N.D. and S.D.-G. contributed equally to this work.

### Notes

The authors declare no competing financial interest.

## ACKNOWLEDGMENTS

This work was supported by the Office of Naval Research (ONR) Award N00014-13-1-0837. F.L., J.L., M.J., and M.A.B. acknowledge partial support by the AFOSR Grant FA9550-14-1-0105 and by the Robert A. Welch Foundation Grant F-1705.

## REFERENCES

- (1) Novoselov, K. S.; Geim, A. K.; Morozov, S. V.; Jiang, D.; Zhang, Y.; Dubonos, S. V.; Grigorieva, I. V.; Firsov, A. A. *Science* **2004**, *306* (5696), 666–669.
- (2) Lemme, M. C.; Echtermeyer, T. J.; Baus, M.; Kurz, H. *IEEE Electron Device Lett.* **2007**, *28* (4), 282–284.
- (3) Novoselov, K. S.; Geim, A. K.; Morozov, S. V.; Jiang, D.; Katsnelson, M. I.; Grigorieva, I. V.; Dubonos, S. V.; Firsov, A. A. *Nature* **2005**, *438* (7065), 197–200.
- (4) Castro Neto, A. H.; Guinea, F.; Peres, N. M. R.; Novoselov, K. S.; Geim, A. K. *Rev. Mod. Phys.* **2009**, *81* (1), 109–162.
- (5) Avouris, P. *Nano Lett.* **2010**, *10* (11), 4285–4294.
- (6) Bao, Q.; Loh, K. P. *ACS Nano* **2012**, *6* (5), 3677–3694.
- (7) Mousavi, S. H.; Kholmanov, I.; Alici, K. B.; Purtseladze, D.; Arju, N.; Tatar, K.; Fozdar, D. Y.; Suk, J. W.; Hao, Y.; Khanikaev, A. B.; Ruoff, R. S.; Shvets, G. *Nano Lett.* **2013**, *13* (3), 1111–1117.
- (8) Yao, Y.; Kats, M. A.; Shankar, R.; Song, Y.; Kong, J.; Loncar, M.; Capasso, F. *Nano Lett.* **2014**, *14* (1), 214–219.
- (9) Yan, H.; Xia, F.; Zhu, W.; Freitag, M.; Dimitrakopoulos, C.; Bol, A. A.; Tulevski, G.; Avouris, P. *ACS Nano* **2011**, *5* (12), 9854–9860.
- (10) Yao, Y.; Kats, M. A.; Genevet, P.; Yu, N.; Song, Y.; Kong, J.; Capasso, F. *Nano Lett.* **2013**, *13* (3), 1257–1264.
- (11) Emani, N. K.; Chung, T.-F.; Kildishev, A. V.; Shalae, V. M.; Chen, Y. P.; Boltasseva, A. *Nano Lett.* **2014**, *14* (1), 78–82.
- (12) Dabidian, N.; Kholmanov, I.; Khanikaev, A. B.; Tatar, K.; Trendafilov, S.; Mousavi, S. H.; Magnuson, C.; Ruoff, R. S.; Shvets, G. *ACS Photonics* **2015**, *2* (2), 216–227.
- (13) Wu, C.; Khanikaev, A. B.; Adato, R.; Arju, N.; Yanik, A. A.; Altug, H.; Shvets, G. *Nat. Mater.* **2011**, *11* (1), 69–75.
- (14) Adato, R.; Yanik, A. A.; Amsden, J. J.; Kaplan, D. L.; Omenetto, F. G.; Hong, M. K.; Erramilli, S.; Altug, H. *Proc. Natl. Acad. Sci. U. S. A.* **2009**, *106* (46), 19227–19232.
- (15) Yu, N.; Capasso, F. *Nat. Mater.* **2014**, *13* (2), 139–150.
- (16) Li, Z.; Yao, K.; Xia, F.; Shen, S.; Tian, J.; Liu, Y. *Sci. Rep.* **2015**, *5*, 12423.
- (17) Liu, X.; Starr, T.; Starr, A. F.; Padilla, W. J. *Phys. Rev. Lett.* **2010**, *104* (20), 207403.
- (18) Shelby, R. A.; Smith, D. R.; Schultz, S. *Science* **2001**, *292* (5514), 77–79.
- (19) Schurig, D.; Mock, J. J.; Justice, B. J.; Cummer, S. A.; Pendry, J. B.; Starr, A. F.; Smith, D. R. *Science* **2006**, *314* (5801), 977–980.
- (20) Fang, N.; Lee, H.; Sun, C.; Zhang, X. *Science* **2005**, *308* (5721), 534–537.
- (21) Ni, X.; Kildishev, A. V.; Shalae, V. M. *Nat. Commun.* **2013**, *4*, 2807.
- (22) Tsai, Y.-J.; Larouche, S.; Tyler, T.; Llopis, A.; Royal, M.; Jokerst, N. M.; Smith, D. R. *Opt. Express* **2013**, *21* (22), 26620–26630.
- (23) Walther, B.; Helgert, C.; Rockstuhl, C.; Setzpfandt, F.; Eilenberger, F.; Kley, E.-B.; Lederer, F.; Tünnermann, A.; Pertsch, T. *Adv. Mater.* **2012**, *24* (47), 6300–6304.
- (24) Huang, L.; Chen, X.; Mühlender, H.; Zhang, H.; Chen, S.; Bai, B.; Tan, Q.; Jin, G.; Cheah, K.-W.; Qiu, C.-W.; Li, J.; Zentgraf, T.; Zhang, S. *Nat. Commun.* **2013**, *4*, 2808.
- (25) Raghunathan, S. B.; Schouten, H. F.; Ubachs, W.; Kim, B. E.; Gan, C. H.; Visser, T. D. *Phys. Rev. Lett.* **2013**, *111* (15), 153901.
- (26) Aieta, F.; Genevet, P.; Kats, M. A.; Yu, N.; Blanchard, R.; Gaburro, Z.; Capasso, F. *Nano Lett.* **2012**, *12* (9), 4932–4936.
- (27) MCLEOD, J. H. J. *Opt. Soc. Am.* **1954**, *44* (8), 592–592.
- (28) Yu, N.; Aieta, F.; Genevet, P.; Kats, M. A.; Gaburro, Z.; Capasso, F. *Nano Lett.* **2012**, *12* (12), 6328–6333.
- (29) Mohsin, M.; Neumaier, D.; Schall, D.; Otto, M.; Matheisen, C.; Lena Giesecke, A.; Sagade, A. A.; Kurz, H. *Sci. Rep.* **2015**, *5*, 10967.
- (30) Midrio, M.; Galli, P.; Romagnoli, M.; Kimerling, L. C.; Michel, J. *Photonics Res.* **2014**, *2* (3), A34.
- (31) Zhou, F.; Hao, R.; Jin, X.-F.; Zhang, X.-M.; Li, E.-P. *IEEE Photonics Technol. Lett.* **2014**, *26* (18), 1867–1870.
- (32) Lee, S. H.; Choi, M.; Kim, T.-T.; Lee, S.; Liu, M.; Yin, X.; Choi, H. K.; Lee, S. S.; Choi, C.-G.; Choi, S.-Y.; Zhang, X.; Min, B. *Nat. Mater.* **2012**, *11* (11), 936–941.
- (33) Emani, N. K.; Chung, T.-F.; Kildishev, A. V.; Shalae, V. M.; Chen, Y. P.; Boltasseva, A. *Nano Lett.* **2014**, *14*, 78.
- (34) Sensale-Rodriguez, B.; Yan, R.; Kelly, M. M.; Fang, T.; Tahy, K.; Hwang, W. S.; Jena, D.; Liu, L.; Xing, H. G. *Nat. Commun.* **2012**, *3*, 780.
- (35) Jang, M. S.; Brar, V. W.; Sherrott, M. C.; Lopez, J. J.; Kim, L.; Kim, S.; Choi, M.; Atwater, H. A. *Phys. Rev. B: Condens. Matter Mater. Phys.* **2014**, *90* (16), 165409.
- (36) Brar, V. W.; Sherrott, M. C.; Jang, M. S.; Kim, S.; Kim, L.; Choi, M.; Sweatlock, L. A.; Atwater, H. A. *Nat. Commun.* **2015**, *6*, 7032.
- (37) Yao, Y.; Shankar, R.; Kats, M. A.; Song, Y.; Kong, J.; Loncar, M.; Capasso, F. *Nano Lett.* **2014**, *14* (11), 6526–6532.
- (38) Emani, N. K.; Chung, T.-F.; Ni, X.; Kildishev, A. V.; Chen, Y. P.; Boltasseva, A. *Nano Lett.* **2012**, *12* (10), 5202–5206.
- (39) Li, Z.; Yu, N. *Appl. Phys. Lett.* **2013**, *102* (13), 131108.
- (40) Peng, F.; Chen, H.; Tripathi, S.; Twieg, R. J.; Wu, S.-T. **2015**; Vol. 9384, p 93840N–93840N–8.
- (41) Chen, H.-T.; Palit, S.; Tyler, T.; Bingham, C. M.; Zide, J. M. O.; O'Hara, J. F.; Smith, D. R.; Gossard, A. C.; Averitt, R. D.; Padilla, W. J.; Jokerst, N. M.; Taylor, A. J. *Appl. Phys. Lett.* **2008**, *93* (9), 091117.
- (42) Khanikaev, A. B.; Wu, C.; Shvets, G. *Nanophotonics* **2013**, *2* (4), 247–264.
- (43) Zhang, S.; Genov, D. A.; Wang, Y.; Liu, M.; Zhang, X. *Phys. Rev. Lett.* **2008**, *101* (4), 047401.

- (44) Lee, Y. G.; Kang, C. G.; Cho, C.; Kim, Y.; Hwang, H. J.; Lee, B. H. *Carbon* **2013**, *60*, 453–460.
- (45) Kim, S.; Nah, J.; Jo, I.; Shahrjerdi, D.; Colombo, L.; Yao, Z.; Tutuc, E.; Banerjee, S. K. *Appl. Phys. Lett.* **2009**, *94* (6), 062107.
- (46) Woessner, A.; Lundeberg, M. B.; Gao, Y.; Principi, A.; Alonso-González, P.; Carrega, M.; Watanabe, K.; Taniguchi, T.; Vignale, G.; Polini, M.; Hone, J.; Hillenbrand, R.; Koppens, F. H. L. *Nat. Mater.* **2014**, *14* (4), 421–425.
- (47) Delfyett, P. J.; Mandridis, D.; Piracha, M. U.; Nguyen, D.; Kim, K.; Lee, S. *Prog. Quantum Electron.* **2012**, *36* (4–6), 475–540.
- (48) Corrigan, P.; Martini, R.; Whittaker, E. A.; Bethea, C. *Opt. Express* **2009**, *17* (6), 4355.
- (49) Li, Y.-M.; An, I.; Nguyen, H. V.; Wronski, C. R.; Collins, R. W. *Phys. Rev. Lett.* **1992**, *68* (18), 2814–2817.
- (50) Li, X.; Zhu, Y.; Cai, W.; Borysiak, M.; Han, B.; Chen, D.; Piner, R. D.; Colombo, L.; Ruoff, R. S. *Nano Lett.* **2009**, *9* (12), 4359–4363.
- (51) Suk, J. W.; Kitt, A.; Magnuson, C. W.; Hao, Y.; Ahmed, S.; An, J.; Swan, A. K.; Goldberg, B. B.; Ruoff, R. S. *ACS Nano* **2011**, *5* (9), 6916–6924.
- (52) Falkovsky, L. A.; Pershoguba, S. S. *Phys. Rev. B: Condens. Matter Mater. Phys.* **2007**, *76* (15), 153410.